

DISCOVERY AND REDSHIFT OF AN OPTICAL AFTERGLOW IN 71 SQUARE DEGREES: iPTF13BXL AND GRB 130702A

LEO P. SINGER¹, S. BRADLEY CENKO², MANSI M. KASLIWAL^{3,13}, DANIEL A. PERLEY^{13,4}, ERAN O. OFEK⁵, DUNCAN A. BROWN^{1,6},
PETER E. NUGENT^{7,8}, S. R. KULKARNI⁴, ALESSANDRA CORSI⁹, DALE A. FRAIL¹⁰, ERIC BELLM⁴, JOHN MULCHAHEY³, IAIR ARCAVI⁵,
TOM BARLOW⁴, JOSHUA S. BLOOM^{7,8}, YI CAO⁴, NEIL GEHRELS², ASSAF HORESH⁴, FRANK J. MASCI¹¹, JULIE MCENERY², ARNE
RAU¹², JASON A. SURACE¹¹, AND OFER YARON⁵

Received 2013 July 20; accepted 2013 September 9; published 2013 October 7

ABSTRACT

We report the discovery of the optical afterglow of the γ -ray burst (GRB) 130702A, identified upon searching 71 deg² surrounding the *Fermi* Gamma-ray Burst Monitor (GBM) localization. Discovered and characterized by the intermediate Palomar Transient Factory, iPTF13bxl is the first afterglow discovered solely based on a GBM localization. Real-time image subtraction, machine learning, human vetting, and rapid response multi-wavelength follow-up enabled us to quickly narrow a list of 27,004 optical transient candidates to a single afterglow-like source. Detection of a new, fading X-ray source by *Swift* and a radio counterpart by CARMA and the Karl G. Jansky Very Large Array confirmed the association between iPTF13bxl and GRB 130702A. Spectroscopy with the Magellan and Palomar 200 inch telescopes showed the afterglow to be at a redshift of $z = 0.145$, placing GRB 130702A among the lowest redshift GRBs detected to date. The prompt γ -ray energy release and afterglow luminosity are intermediate between typical cosmological GRBs and nearby sub-luminous events such as GRB 980425 and GRB 060218. The bright afterglow and emerging supernova offer an opportunity for extensive panchromatic follow-up. Our discovery of iPTF13bxl demonstrates the first observational proof-of-principle for ~ 10 *Fermi*-iPTF localizations annually. Furthermore, it represents an important step toward overcoming the challenges inherent in uncovering faint optical counterparts to comparably localized gravitational wave events in the Advanced LIGO and Virgo era.

Subject headings: gamma-ray burst: individual (GRB 130702A)

1. INTRODUCTION

Our understanding of γ -ray bursts (GRBs) has been propelled by our ability to localize these rare and energetic cosmic events precisely. *Compton Gamma-ray Observatory*/BATSE's coarse localizations robustly demonstrated that GRBs were distributed isotropically on the sky and suggested that GRBs originate at cosmological distances (Meegan et al. 1992). Prompt arcminute localizations provided by *Bep-poSAX* directly enabled the discovery of the first afterglows of long-duration GRBs (Costa et al. 1997; van Paradijs et al.

1997; Frail et al. 1997). Currently, the prompt slewing capabilities of the *Swift* satellite (Gehrels et al. 2004) enable the on-board narrow-field instruments to provide arcsecond localizations for ≈ 90 GRBs yr⁻¹ within ≈ 100 s of the burst trigger.

With seven decades of simultaneous energy coverage, *Fermi* has opened a new window into the GRB phenomenon, the MeV to GeV regime. However, *Fermi* remains fundamentally limited by its localization capabilities. The Large Area Telescope (LAT; 20 MeV–300 GeV; 16% of all-sky; Atwood et al. 2009) can localize events with GeV photons to radii as small as $\sim 10'$. But the LAT only localizes a handful of GRBs each year. The Gamma-ray Burst Monitor (GBM; few keV–30 MeV; 70% of all-sky; Meegan et al. 2009), on the other hand, detects GRBs at a rate of ≈ 250 yr⁻¹. However, typical GBM GRBs have localizations of many tens of square degrees (random plus systematic uncertainties). Consequently, no afterglows have been identified based solely on a GBM localization until this work¹⁴.

The Palomar Transient Factory (PTF; Law et al. 2009) is developing the necessary instrumentation, algorithms, and observational discipline to detect optical counterparts to GBM GRBs. The wide 7.1 deg² field of view and sensitivity ($R \approx 20.6$ mag in 60 s) of the P48 and CFHT12k camera (Rahmer et al. 2008) are well-suited to identifying long-duration GRB afterglow candidates. The real-time software pipeline (Nugent et al., in prep.) enables rapid panchromatic follow-up with an arsenal of telescopes (e.g. Gal-Yam et al. 2011), essential to distinguish the true afterglow from background and

lsinger@caltech.edu

¹ LIGO Laboratory, California Institute of Technology, Pasadena, CA 91125, USA

² Astrophysics Science Division, NASA Goddard Space Flight Center, Mail Code 661, Greenbelt, MD 20771, USA

³ Observatories of the Carnegie Institution for Science, 813 Santa Barbara St, Pasadena CA 91101, USA

⁴ Cahill Center for Astrophysics, California Institute of Technology, Pasadena, CA 91125, USA

⁵ Benoziyo Center for Astrophysics, The Weizmann Institute of Science, Rehovot 76100, Israel

⁶ Department of Physics, Syracuse University, Syracuse, NY 13244, USA

⁷ Department of Astronomy, University of California Berkeley, B-20 Hearst Field Annex # 3411, Berkeley, CA, 94720-3411

⁸ Physics Division, Lawrence Berkeley National Laboratory, 1 Cyclotron Road MS 50B-4206, Berkeley, CA 94720, USA

⁹ George Washington University, Corcoran Hall, Washington, DC 20052, USA

¹⁰ National Radio Astronomy Observatory, P.O. Box O, Socorro, NM 87801, USA

¹¹ Infrared Processing and Analysis Center, California Institute of Technology, Pasadena, CA 91125, USA

¹² Max-Planck-Institut für extraterrestrische Physik, Giessenbachstrasse 1, 85748 Garching, Germany

¹³ Hubble Fellow

¹⁴ The only comparable discovery was the afterglow of GRB 120716A in the ≈ 2 deg² error box from the InterPlanetary Network (IPN) by Cenko et al. (2012).

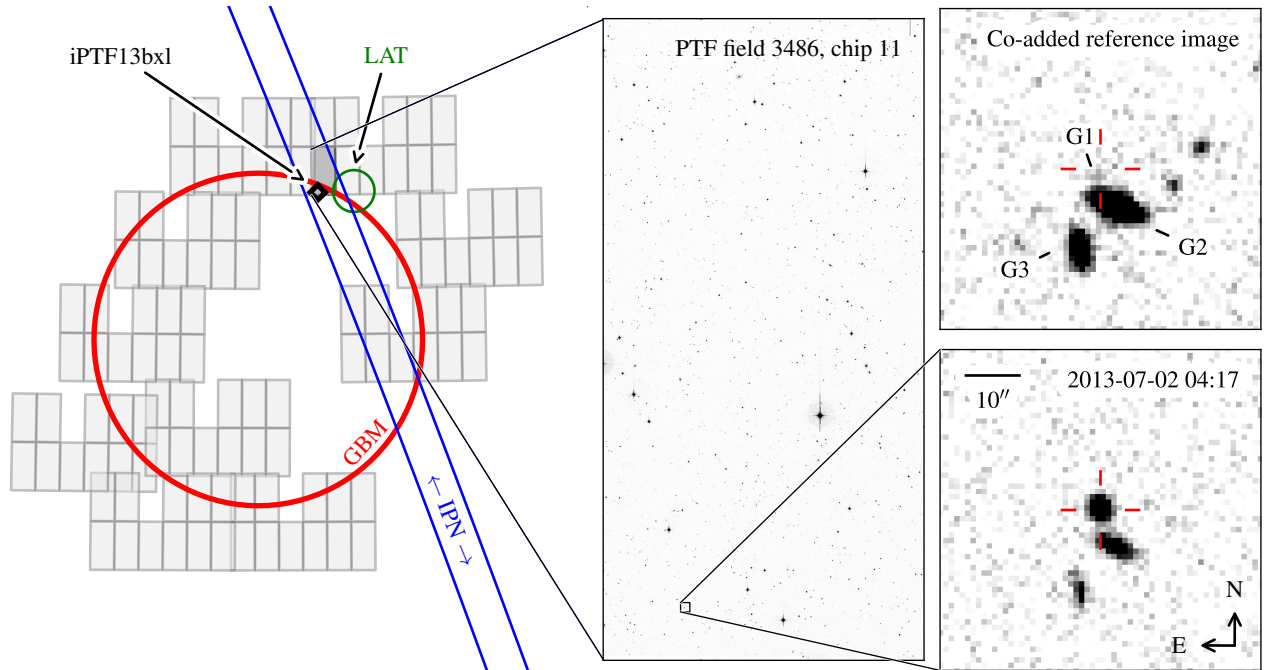


Figure 1. P48 imaging of GRB 130702A and discovery of iPTF13bxl. The left panel illustrates the γ -ray localizations (red circle: 1σ GBM; green circle: LAT; blue lines: 3σ IPN) and the 10 Palomar 48 inch Oschin telescope (P48) reference fields that were imaged (light gray rectangles). For each P48 pointing, the location of the 11 chips are indicated with smaller rectangles (one CCD in the camera is not currently operable). Our tiling algorithm places a large weight on the existence of deep P48 pre-explosion imaging (a necessity for high-quality subtraction images); the large gaps inside the GBM localization are fields without these reference images. The small black diamond is the location of iPTF13bxl. The right panels show P48 images of the location of iPTF13bxl, both prior to (top) and immediately following (bottom) discovery. We note that the LAT and IPN localizations were published *after* our discovery announcement (Singer et al. 2013). (A color version of this figure is available in the online journal.)

foreground contaminants. Here, we present our discovery of iPTF13bxl, the afterglow of the *Fermi* GBM GRB 130702A found by searching a sky area of 71 deg^2 with the intermediate Palomar Transient Factory (iPTF).

2. DISCOVERY

On 2013 July 2 at 00:05:23.079 UT, the *Fermi* GBM detected trigger 394416326. The refined human-generated (i.e., ground-based) localization, centered on $\alpha = 14^{\text{h}}35^{\text{m}}14^{\text{s}}$, $\delta = 12^{\circ}15'00''$ (J2000.0), with a quoted 68% containment radius of 4.0 (statistical uncertainty only), was disseminated less than an hour after the burst (Figure 1).

Fermi-GBM GRB positions are known to suffer from significant systematic uncertainties, currently estimated to be $\approx 2^{\circ}$ – 3° . To characterize the full radial profile of the localization uncertainty, our GBM-iPTF pipeline automatically computed a probability map for the event modeled on previous *Fermi*/*Swift* coincidences from 2010 March 30 through 2013 April 4. We fit a sigmoid function:

$$P(r) = \frac{1}{1 + (c_0 r)^{c_1}} \quad (1)$$

where r is the angular distance to the *Swift* location, normalized by the in-flight or ground-based error radius for that burst. We find $c_0 = 1.35$, $c_1 = -2.11$ for in-flight GBM localizations and $c_0 = 0.81$, $c_1 = -2.47$ for ground-based GBM localizations (Figure 2).

Image subtraction within iPTF is greatly simplified by observing only pre-defined fields on the sky; this ensures that sources will fall on approximately the same detector location from night to night, minimizing a possible source of system-

atic uncertainty. Using a Hierarchical Equal Area isoLatitude Pixelization (HEALPix; Górski et al. 2005) bitmap representation of the probability distribution of the trigger location, we chose 10 of these pre-defined fields to maximize the probability of enclosing the true (but still unknown) location of the burst (Figure 1). In this particular case, the ten selected fields did not include the center of the GBM localization because we lacked previous reference images there. Nonetheless, we estimated that these ten fields had a 38% chance of containing this GRB’s location. Given the youth, sky location, and probability of containment, we let our software trigger follow-up with the P48.

Starting at 04:17:23 UT ($\Delta t \equiv t - t_{\text{GBM}} = 4.2 \text{ hr}$), we imaged each of these ten fields twice in 60 s exposures with the Mould R filter. These fields were then subjected to the standard iPTF transient search: image subtraction, source detection, and “real/bogus” machine ranking (Bloom et al. 2012; Brink et al. 2013) into likely astrophysical transient sources (“real”, or 1) or likely artifacts (“bogus”, or 0).

The iPTF real-time analysis found 27,004 transient/variable candidates in these twenty individual subtracted images. Of these, 44 were eliminated because they were determined to be known asteroids in the Minor Planet Checker database¹⁵ using PyMPChecker.¹⁶ Demanding a real/bogus rank greater than 0.1 reduced the list to 4214. Rejecting candidates that coincided with point sources in Sloan Digital Sky Survey (SDSS) brighter than $r' = 21$ narrowed this to 2470. Further requiring detection in both P48 visits and imposing CCD-wide data quality cuts (e.g., bad pixels) eliminated all but 43 candidates.

¹⁵ <http://www.minorplanetcenter.org/iau/mpc.html>

¹⁶ <http://dotastro.org/PyMPC/PyMPC/>

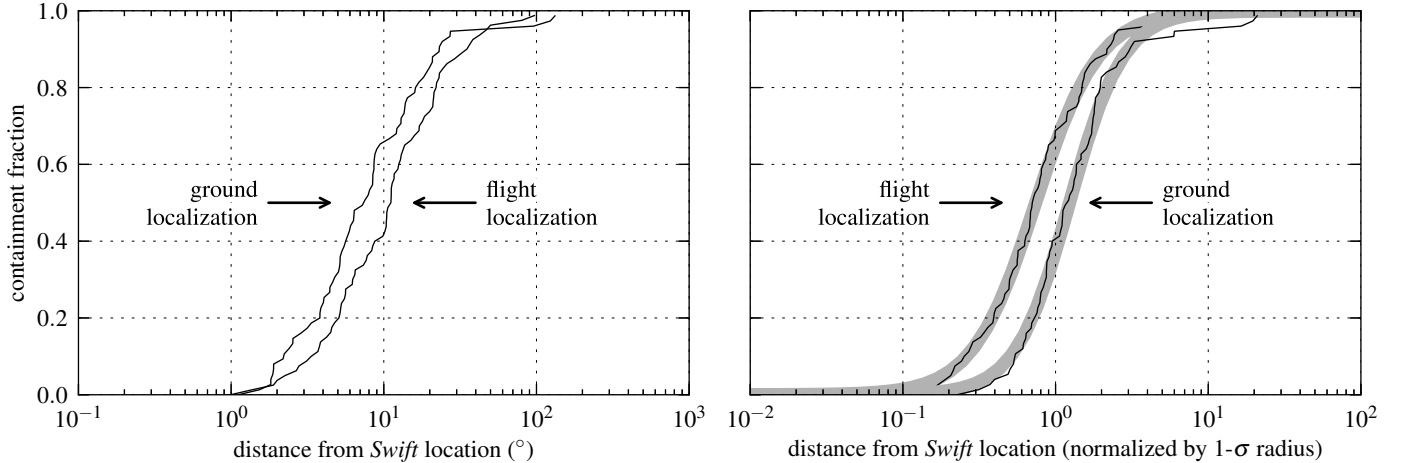


Figure 2. Localization accuracy of *Fermi* GBM positions, generated by searching for coincidences with GRBs detected by the *Swift* satellite. The left panel shows the fraction of bursts contained within a given distance from the *Swift* position, both for in-flight and refined ground-based localizations. Ground-based localizations are on average about half as far from the true GRB positions as the in-flight localizations. The right panel shows a cumulative histogram of the *Fermi*–*Swift* distance, normalized by each trigger’s nominal 1σ radius (either ground-based or in-flight). Although the ground-based localizations are more accurate, the nominal ground-based error radii must be interpreted as describing a different confidence level than the in-flight error radius. The thick gray lines are fits to the logistic-like function in Equation 1.

Following human inspection, seven sources were saved as promising transients in the iPTF database.

Two candidates, iPTF13bxh and iPTF13bxu, were near the cores of bright, nearby galaxies, environments that are inherently variable and also present a challenge to image subtraction. A third, iPTF13bxr, was coincident with a galaxy in SDSS with a quasar spectrum (SDSS J145359.72+091543.3). iPTF13bxt was close to a star in SDSS, and so was deemed a likely variable star. We did not consider these further for the afterglow search. The final three sources, iPTF13bxj (real-bogus score = 0.86), iPTF13bxk (real-bogus score = 0.49), and iPTF13bxl (real-bogus score = 0.83), remained as potential counterparts and were scheduled for $g'r'i'$ photometry with the Palomar 60 inch telescope (P60; Cenko et al. 2006) and spectroscopic classification on the Palomar 200 inch telescope (P200). iPTF13bxl ($\alpha = 14^{\text{h}}29^{\text{m}}14^{\text{s}}.78$, $\delta = +15^{\circ}46'.26''$) was immediately identified as the most promising candidate because it showed a significant intra-night decline. Our panchromatic follow-up (Sections 3 and 4) confirmed iPTF13bxl was indeed the afterglow. Subsequent spectroscopy revealed iPTF13bxj to be a Type II supernova at $z = 0.06$ and iPTF13bxk a quasar at $z = 2.4$.

Following our discovery announcement (Singer et al. 2013), the *Fermi* LAT and GBM teams published GRB Coordinates Network (GCN) circulars announcing the detection of GRB 130702A (Cheung et al. 2013; Collazzi & Connaughton 2013). As seen by the GBM, GRB 130702A had a duration of $t_{90} \approx 59$ s and a 10 keV–1 MeV fluence of $f_{\gamma} = (6.3 \pm 2.0) \times 10^{-6}$ erg cm $^{-2}$. The best-fit power-law spectrum may suggest a classification as an X-ray flash. The LAT location was $0^{\circ}.9$ from iPTF13bxl, with a 90% statistical error radius of $0^{\circ}.5$. An IPN triangulation (Hurley et al. 2013) yielded a $3\text{-}\sigma$ annulus that was $0^{\circ}.46$ wide from its center to its edges. iPTF13bxl was $0^{\circ}.16$ from the annulus’ centerline (Figure 1).

3. BROADBAND PHOTOMETRIC FOLLOW-UP

On 2013 July 3 at 4:10 UT, ($\Delta t = 28.1$ hr), the P60 obtained two sequences of Sloan $g'r'i'$ observations of the field of iPTF13bxl. P60 observations were calibrated relative to 20 reference stars in the SDSS (AB) system. Final reduction of the P48 observations was performed automatically

at the Infrared Processing and Analysis Center (Ofek et al. 2012). We corrected the P48 and P60 photometry for Galactic extinction using maps from Schlafly & Finkbeiner (2011, $E(B - V) = 0.024$ mag).

The optical light curve is shown in Figure 3. We fit an achromatic broken power law to all filters and all times up to $\Delta t = 5$ days after the burst. A spectral slope of $\beta_{\text{O}} = 0.7 \pm 0.1$ is sufficient to characterize the post-break color, illustrated in the inset of Figure 4. We note that the optical decay ceased at $r' \approx 20$ mag after $\Delta t \approx 5$ days when the accompanying supernova started to dominate (Schulze et al. 2013). This supernova will be the subject of a future work.

Following our discovery of iPTF13bxl, we triggered target of opportunity observations with the *Swift* XRT (Burrows et al. 2005) beginning at 00:50 UT on 2013 July 3 ($\Delta t = 1.03$ days). We downloaded the data products from the *Swift* XRT repository (Evans et al. 2007). The resulting 0.3–10 keV light curve is plotted in Figure 3. The spectrum is well fit by a power law with photon index $\Gamma = 2.0^{+0.14}_{-0.13}$, while the light curve fades in time with a power-law slope of $\alpha_{\text{X}} = 1.06 \pm 0.02$, in excellent agreement with the post-break optical decay.

After the discovery of the optical counterpart to GRB 130702A, we began observations with the Combined Array for Research in Millimeter-wave Astronomy (CARMA). All observations were carried out in single-polarization mode with the 3 mm receivers tuned to a frequency of 93 GHz, and were reduced using MIRIAD. We flux-calibrated the data using observations of MWC349 and 3C273. The afterglow is well-detected in both epochs, and we measure flux densities of 1.58 ± 0.33 mJy and 1.85 ± 0.30 mJy on July 4.13 and 5.17, respectively.

The position of iPTF13bxl was observed with the Karl G. Jansky Very Large Array (VLA) in C-band beginning at 6:20 UT on 2013 July 4 ($\Delta t = 2.29$ days). The observations were conducted using the standard WIDAR correlator setting. Data were reduced using the Astronomical Image Processing System package following standard practice. 3C286 was used for bandpass and flux calibration; J1415+1320 was used for gain and phase calibration. We detect a radio source with flux density of 1.49 ± 0.08 mJy at 5.1 GHz at 1.60 ± 0.08 mJy at

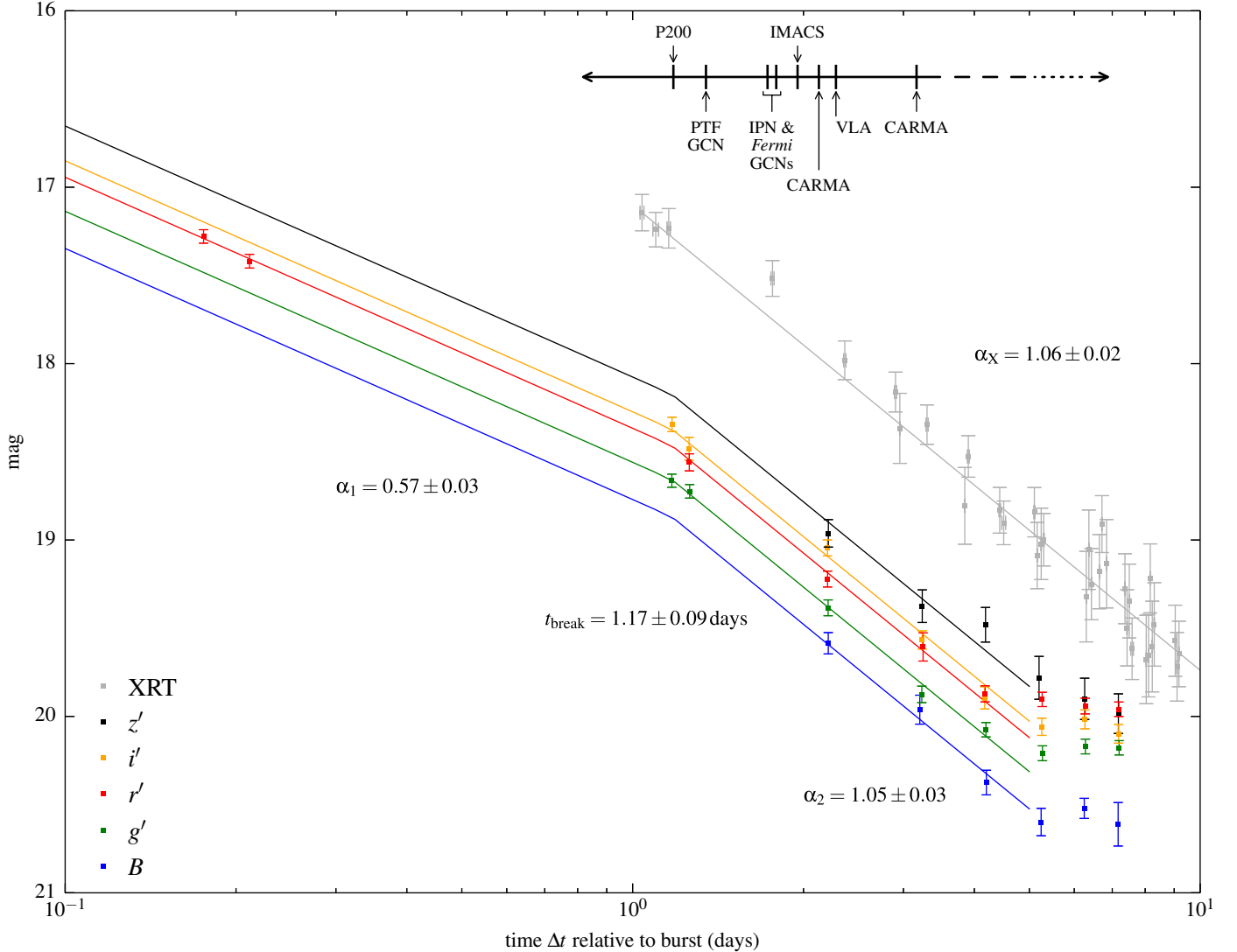


Figure 3. P48, P60, and X-Ray Telescope (XRT) light curves of iPTF13bxl. The broken power-law fit is shown up to $\Delta t = 5$ days. The XRT observations, re-binned to improve presentation, are shown in gray as $m(\text{AB}) - 6.5$ at 1 keV. A timeline in the top right puts the P48 and P60 observations in the context of the XRT follow-up, PTF’s discovery GCN (Singer et al. 2013), the announcement of the LAT (Cheung et al. 2013) and IPN (Hurley et al. 2013) localizations, and the radio observations. (A color version of this figure is available in the online journal.)

7.1 GHz. Errors on the measured flux were calculated as the quadrature sum of the map root-mean square and a fractional systematic error (of the order of 5%) to account for uncertainty in the flux density calibration.

The broadband spectral energy distribution (SED) is shown in Figure 4. We interpolated both the optical and X-ray observations to the mean time of the VLA and CARMA observations. In the context of the standard synchrotron afterglow model (Sari et al. 1998), the comparable X-ray and optical spectral and temporal indices at this time suggest both bandpasses lie in the same spectral regime, likely with $\nu > \nu_c$. This would imply a relatively hard electron spectral energy index ($N(\gamma_e) \propto \gamma_e^{-p}$) $p \approx 2$, possibly requiring a high-energy cut-off.

Also in Figure 4 we plot three broadband SED models synthesized using techniques similar to Perley et al. (2013). Although these models are not formal fits to our highly under-constrained observations, they demonstrate overall consistency with standard synchrotron afterglow theory. Model

“A” (dashed line; $\chi^2 = 126$) represents a constant-density (ISM) circumburst medium with $p = 2.1$, $\epsilon_B = 0.48$, $\epsilon_e = 0.41$, $E = 3 \times 10^{51}$ erg, $n = 1.2 \times 10^{-3} \text{ cm}^{-3}$. This model underpredicts the VLA bands, but this deviation could be due to scintillation or reverse shock emission at low frequencies. Model “B” (dotted line; $\chi^2 = 7$) is in a wind environment ($\rho \propto r^{-2}$) with $p = 2.1$, $\epsilon_B = 0.32$, $\epsilon_e = 0.43$, $E = 1.4 \times 10^{51}$ erg, $A_* = 4.8 \times 10^{-3} \text{ g cm}^{-1}$. This fits the data well except for a small discrepancy with the optical spectral slope. Model “C” (dotted-dashed line; $\chi^2 = 6$) is a similar wind model but with $p = 1.55$. Of the three, “C” fits the data best, but seems non-physical (high-energy cutoff required). Accurate determination of the underlying physical parameters would require tracing the evolution of the SED with time.

4. OPTICAL SPECTROSCOPY AND HOST GALAXY ENVIRONMENT

We obtained optical spectra of iPTF13bxl with the Double Spectrograph (DBSP) mounted on the P200 on

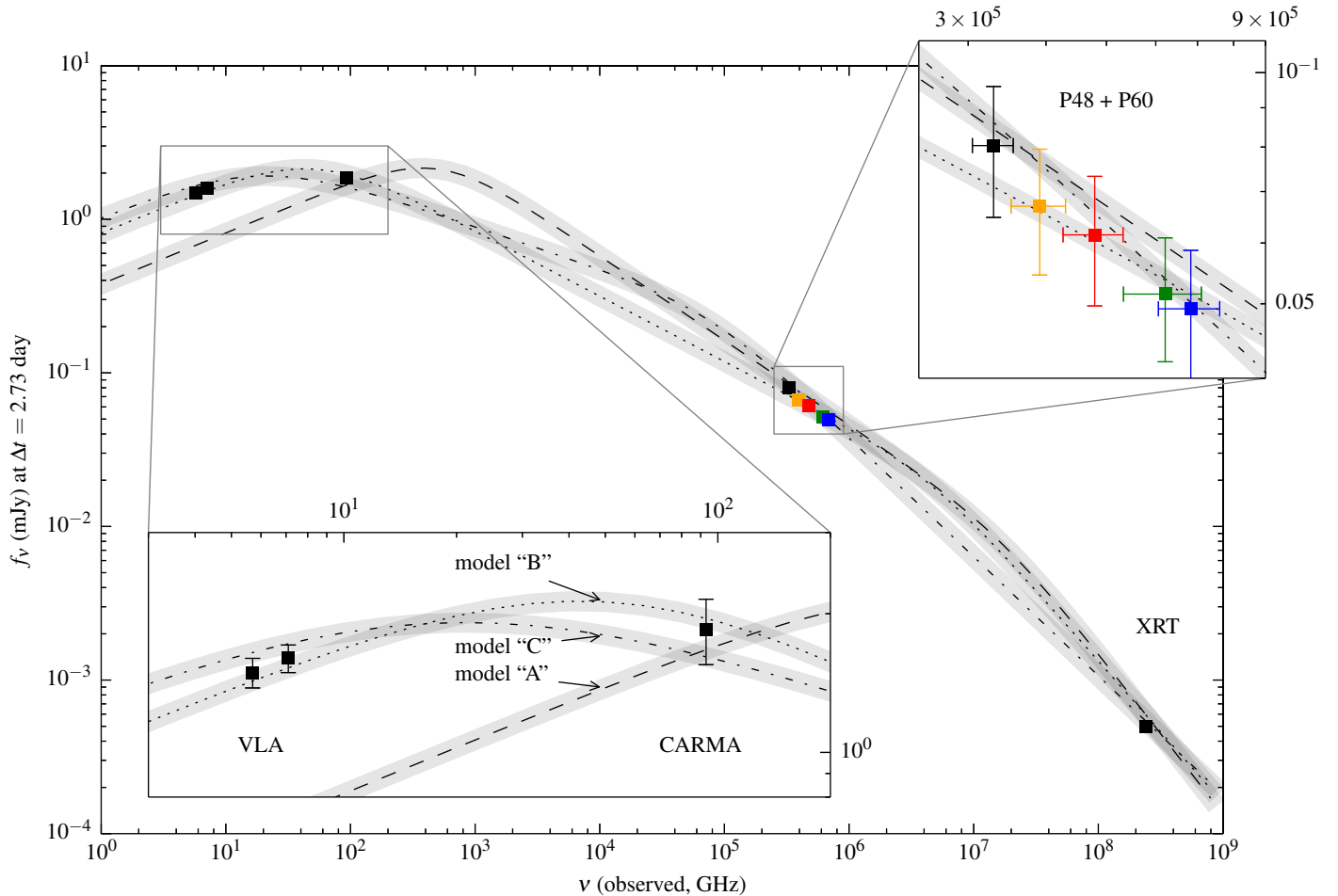


Figure 4. Broadband SED of iPTF13bx1. Two insets show details of the radio and optical observations respectively. The XRT and optical observations have been interpolated to the mean time of the radio observations ($\Delta t = 2.6$ days). (A color version of this figure is available in the online journal.)

2013 July 3.17 and the Inamori-Magellan Areal Camera & Spectrograph (IMACS; Dressler et al. 2011) mounted on the 6 m Magellan Ba’ade telescope on 2013 July 3.97 ($\Delta t = 1.2$ and 2.0 days, respectively). The resulting spectra are plotted in Figure 5.

Our initial DBSP spectrum exhibits a largely featureless, blue continuum. The higher signal-to-noise ratio (S/N) of the IMACS spectrum further reveals faint, narrow emission lines corresponding to [O III] and $H\alpha$ at a common redshift of $z = 0.145 \pm 0.001$ (luminosity distance $d_L = 680$ Mpc), which we adopt as the distance to GRB 130702A. The continuum of both spectra exhibit deviations from a single power-law, with excess flux (when compared with the late-time photometric spectral index of $\beta_0 = 0.7$) visible at shorter wavelengths. This may suggest some contribution from either shock breakout or the emerging supernova at very early times post-explosion.

Three galaxies are visible in the immediate environment of iPTF13bx1 in pre-explosion imaging (labeled “G1”, “G2”, and “G3” in Figure 1). Presumably the emission lines observed from iPTF13bx1 arise in G1, given the small spatial offset ($0''.6$) and slit orientation (PA = 90). However, our spectra also reveal galaxies G2 and G3 both lie at redshifts consistent with iPTF13bx1 (e.g., Figure 5). Observations with DEIMOS on the Keck II telescope reveal two more galaxies at the same redshift at separations of $1/2$ (SDSS J142910.29+154552.2)

and $2/7$ (SDSS J142917.67+154352.2) from the transient. The explanation most consistent with past observations of long-duration GRB host galaxies (e.g., Savaglio et al. 2009) is that GRB 130702A exploded in a dwarf ($M_r \approx -16$ mag) member of this association or group, a relatively unusual environment (see also Kelly et al. 2013).

5. GRB 130702A IN CONTEXT

The prompt γ -ray isotropic energy release ($E_{\gamma, \text{iso}}$) of GRBs spans a range of six orders of magnitude, from $\sim 10^{48}$ – 10^{54} erg. At $z = 0.145$, the prompt emission from GRB 130702A constrains $E_{\gamma, \text{iso}} \lesssim (6.5 \pm 0.1) \times 10^{50}$ erg (90% upper limit; Amati et al. 2013). This value is significantly smaller than typical cosmological GRBs ($E_{\gamma, \text{iso}} \sim 10^{52}$ – 10^{54} erg; Amati 2006; Butler et al. 2007). Yet GRB 130702A greatly outshines the most nearby, sub-luminous events with well-studied supernovae, such as GRB 980425 ($E_{\gamma, \text{iso}} = 1.0 \times 10^{48}$ erg; Pian et al. 2000) and GRB 060218 ($E_{\gamma, \text{iso}} = 6.2 \times 10^{49}$ erg; Campana et al. 2006).

At all wavelengths, the counterpart behaves like a typical GRB afterglow scaled down in luminosity by a factor of ~ 10 compared to a “typical” *Swift* burst (or ~ 100 lower than a luminous pre-*Swift* burst) as observed at the same time. This is intuitively explained by an equivalent scaling down of the overall energy (per solid angle) of the burst and shockwave relative to more typical, high-luminosity bursts. It is not yet

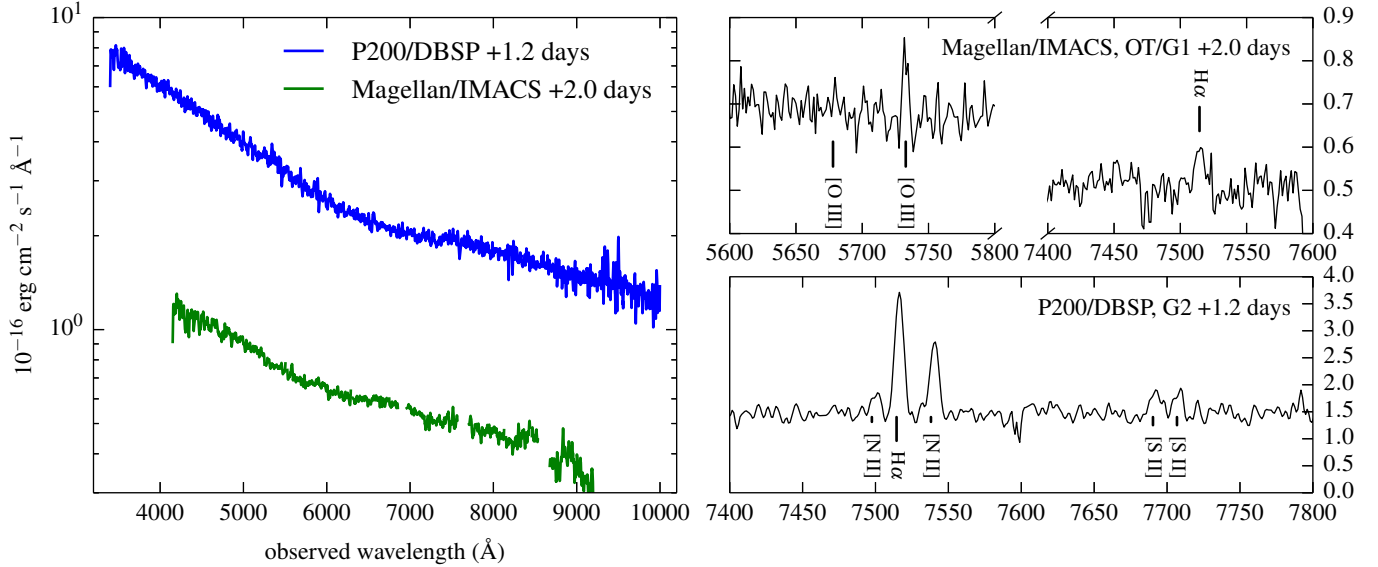


Figure 5. Optical spectra of iPTF13btl and the nearby galaxy SDSS J142914.57+154619.3 (“G2”). Spectra in the left panel have been smoothed with a Savitzky-Golay filter. Our initial P200 spectrum of the afterglow (left panel, blue) exhibits a largely featureless blue continuum. A higher S/N spectrum taken the following night with IMACS (left panel, green) revealed faint emission features corresponding to [O III] and H α at $z = 0.145$ (top right panel). The bottom right panel shows a spectrum of the nearby galaxy G2, which has the same redshift as iPTF13btl. (A color version of this figure is available in the online journal.)

clear whether this energy difference is due primarily to the release of less relativistic ejecta by the burst overall, a wider jet, or a partially off-axis view of a structured jet. Late-time radio follow-up should help distinguish these models: an intrinsically low-energy GRB should produce a much earlier jet break than a widely-beamed burst, while a structured jet will actually produce an *increase* in flux at late times as the jet core spreads and its radiation enters our sightline.

Events with similar energetics have been found by *Swift*, e.g., GRB 050826 at $z = 0.30$ and GRB 120422A at $z = 0.28$ (Mirabal et al. 2007; Zhang et al. 2012). However, given their low intrinsic luminosities and higher redshift, the afterglows were too faint to identify late-time breaks and establish their shock energies E_K , making them difficult to physically interpret. GRB 130702A’s proximity avoids both these problems. Our observations suggest—and further observations should confirm—that its γ -ray and afterglow energetics are intermediate between these two previously quite-disparate classes of GRBs, helping to fill in the “gap” between the well-studied cosmological population and the class of less-luminous local GRBs and relativistic Type Ic supernovae (e.g., Soderberg et al. 2004, 2010).

6. CONCLUSION

Using the infrastructure outlined above, we estimate that a dedicated iPTF program would recover ~ 10 GBM afterglows each year. The addition of other surveys with comparably wide field of views and apertures (e.g., Pan-STARRS, SkyMapper, CRTS) could increase this number, assuming they had similar real-time transient detection and follow-up programs in place. Since GBM detects GRBs in the classical γ -ray band, their optical counterparts should more closely resemble the pre-*Swift* population (≈ 1 mag brighter at a fixed time; Kann et al. 2010). Even if only a single event per year as nearby as GRB 130702A were uncovered, this would still represent a remarkable advance in our understanding of the GRB–supernova connection.

Furthermore, this work sets the stage for more discoveries in ongoing and future physics experiments that are limited by

similarly coarse position reconstruction. Later this decade, a network of advanced gravitational wave (GW) detectors including the Laser Interferometer GW Observatory (LIGO) and Virgo is expected to detect ~ 0.4 –400 binary neutron star mergers per year (Abadie et al. 2010), but with positions uncertain to tens to hundreds of deg^2 (Fairhurst 2011; Nissanke et al. 2011; Aasi et al. 2013).

Optical counterparts to GW sources will rarely (due to jet collimation) include bright, on-axis short-hard burst afterglows. Fainter r -process–fueled kilonovae (Li & Paczyński 1998) or yet fainter off-axis afterglows (Rhoads 1997) are expected to accompany binary neutron star mergers. Both of these signatures are predicted to be several magnitudes fainter than iPTF13btl. Optical searches will be inundated with astrophysical false positives (Nissanke et al. 2013). This problem will only be exacerbated for future surveys covering larger areas (e.g., Zwicky Transient Facility; Kulkarni 2012) and/or with larger apertures (e.g., Large Synoptic Survey Telescope; Tyson 2002). However, a breathtakingly complete astrophysical picture could reward us: masses and spins measured in GWs; host galaxy and disruption ejecta in optical; circumstellar environment in radio. The case of GRB 130702A demonstrates for the first time that optical transients can be recovered from localization areas of $\sim 100 \text{ deg}^2$, reaching a crucial milestone on the road to Advanced LIGO.

Optical photometry and spectroscopy referred to in this work will be made available via WISerEP¹⁷ (Yaron & Gal-Yam 2012).

We acknowledge A. Weinstein, A. Gal-Yam, R. Quimby, V. Connaughton, and the *Fermi*-GBM team for valuable discussions, S. Caudill, S. Tinyanont, D. Khatami for P200 observing, and the developers of the COSMOS package for Magellan data reduction.

This research is supported by the National Science Foundation through a Graduate Research Fellowship for

¹⁷ <http://www.weizmann.ac.il/astrophysics/wiserep/>

L.P.S., award PHY-0847611 for D.A.B., and NSF-CDI grant 0941742 for J.S.B. M.M.K. acknowledges generous support from the Carnegie-Princeton Fellowship. M.M.K. and D.A.P. are supported by NASA through the Hubble Fellowship grants HST-HF-51293.01 and HST-HF-51296.01-A, awarded by the Space Telescope Science Institute, which is operated by the Association of Universities for Research in Astronomy, Inc., for NASA, under contract NAS 5-26555. E.O.O. is the incumbent of the Arye Dissentshik career development chair and is supported by grants from the Israeli Ministry of Science and the I-CORE Program. D.A.B. is further supported by an RCSA Cottrell Scholar award.

This research made use of Astropy (Robitaille et al. 2013, <http://www.astropy.org>), a community-developed core Python package for Astronomy. The National Radio Astronomy Observatory is a facility of the National Science Foundation operated under cooperative agreement by Associated Universities, Inc.

REFERENCES

- Aasi, J., et al. 2013
 Abadie, J., et al. 2010, *CQGra*, 27, 173001
 Amati, L. 2006, *MNRAS*, 372, 233
 Amati, L., et al. 2013, *GCN*, 15025, 1
 Atwood, W. B., et al. 2009, *ApJ*, 697, 1071
 Bloom, J. S., et al. 2012, *PASP*, 124, 1175
 Brink, H., et al. 2013, *MNRAS* (in press)
 Burrows, D. N., et al. 2005, *SSRv*, 120, 165
 Butler, N. R., et al. 2007, *ApJ*, 671, 656
 Campana, S., et al. 2006, *Nature*, 442, 1008
 Cenko, S. B., Ofek, E. O., & Nugent, P. E. 2012, *GCN*, 13489, 1
 Cenko, S. B., et al. 2006, *PASP*, 118, 1396
 Cheung, T., et al. 2013, *GCN*, 14971, 1
 Collazzi, A. C., & Connaughton, V. 2013, *GCN*, 14972, 1
 Costa, E., et al. 1997, *Nature*, 387, 783
 Dressler, A., et al. 2011, *PASP*, 123, 288
 Evans, P. A., et al. 2007, *A&A*, 469, 379
 Fairhurst, S. 2011, *CQGra*, 28, 105021
 Frail, D. A., et al. 1997, *Nature*, 389, 261
 Gal-Yam, A., et al. 2011, *ApJ*, 736, 159
 Gehrels, N., et al. 2004, *ApJ*, 611, 1005
 Górski, K. M., et al. 2005, *ApJ*, 622, 759
 Hurley, K., et al. 2013, *GCN*, 14974, 1
 Kann, D. A., et al. 2010, *ApJ*, 720, 1513
 Kelly, P. L., et al. 2013, *ApJ*, 775, L5
 Kulkarni, S. R. 2012, in *Proceedings of the International Astronomical Union*, Vol. 285, IAU Symposium, ed. E. Griffin, R. Hanisch, & R. Seaman, 55–61
 Law, N. M., et al. 2009, *PASP*, 121, 1395
 Li, L.-X., & Paczyński, B. 1998, *ApJ*, 507, L59
 Meegan, C., et al. 2009, *ApJ*, 702, 791
 Meegan, C. A., et al. 1992, *Nature*, 355, 143
 Mirabal, N., Halpern, J. P., & O'Brien, P. T. 2007, *ApJ*, 661, L127
 Nissanke, S., Kasliwal, M., & Georgieva, A. 2013, *ApJ*, 767, 124
 Nissanke, S., et al. 2011, *ApJ*, 739, 99
 Ofek, E. O., et al. 2012, *PASP*, 124, 62
 Perley, D. A., et al. 2013, *ApJ* submitted (astro-ph/1307.4401)
 Pian, E., et al. 2000, *ApJ*, 536, 778
 Rahmer, G., et al. 2008, in *Proc. SPIE*, Vol. 7014, 70144Y–70144Y–12
 Rhoads, J. E. 1997, *ApJ*, 487, L1
 Robitaille, T. P., et al. 2013, *A&A*, 558, A33
 Sari, R., Piran, T., & Narayan, R. 1998, *ApJ*, 497, L17
 Savaglio, S., Glazebrook, K., & Le Borgne, D. 2009, *ApJ*, 691, 182
 Schlafly, E. F., & Finkbeiner, D. P. 2011, *ApJ*, 737, 103
 Schulze, S., et al. 2013, *GCN*, 14994, 1
 Singer, L. P., et al. 2013, *GCN*, 14967, 1
 Soderberg, A. M., et al. 2004, *Nature*, 430, 648
 —. 2010, *Nature*, 463, 513
 Tyson, J. A. 2002, in *Proc. SPIE*, ed. J. A. Tyson & S. Wolff, Vol. 4836, 10–20
 van Paradijs, J., et al. 1997, *Nature*, 386, 686
 Yaron, O., & Gal-Yam, A. 2012, *PASP*, 124, 668
 Zhang, B.-B., et al. 2012, *ApJ*, 756, 190